Large Anomalous Hall Effect in Double-Q Magnets without Net Scalar Spin Chirality

Satoru Ohgata[1] and Satoru Hayami[1]

[1] *Graduate School of Science, Hokkaido University, Sapporo 060-0810, Japan.*

Multi-Q magnets consist of superposed spin-density waves with distinct magnetic modulation vectors, enabling a wide range of magnetic orders depending on their combination. Among them, topologically nontrivial spin textures, such as a magnetic skyrmion, have been extensively studied owing to the emergence of topological Hall effects induced by real-space scalar spin chirality. Contrary to this expectation, we theoretically investigate another route to enhancing the Hall response under a topologically trivial double-Q spin textures with neither net scalar spin chirality nor a nonzero skyrmion number. Despite the cancellation of the scalar spin chirality, the double-Q magnetism exhibits a Hall response significantly larger than that of the ferromagnetic phase with a nonmonotonic dependence on the uniform magnetization, which is in stark contrast with a ferromagnetic state and a single-Q spiral state. Analyzing the multiorbital Kondo lattice model, we show that orbital hybridization induced by the double-Q superstructure results in a proliferation of Berry curvature hot spots in $\boldsymbol{k}$ space, thereby giving rise to a large anomalous Hall effect. This mechanism accounts for the observed giant anomalous Hall effect in $GdRu_2Si_2$ and $GdRu_2Ge_2$, thereby highlighting topologically trivial double-Q spin textures as promising spintronic materials.

Multi-Q magnets are systems in which multiple spin-density waves (SDWs) with distinct magnetic modulation vectors $\boldsymbol{Q}$ are superposed [1–3]. Depending on the combination of SDWs involved, multi-Q magnets can realize a wide range of magnetic orders [4–8]. Among these, noncoplanar spin textures are of particular interest due to their finite scalar spin chirality in real space [9, 10]. This scalar spin chirality acts as an emergent magnetic field, which induces a transverse current even without an external magnetic field or relativistic spin-orbit coupling (SOC), i.e., the topological Hall effect (THE) [11–20]. Topologically nontrivial spin textures—such as skyrmions—have attracted considerable attention [19, 21–25], since the skyrmion number

$$N_{\rm sk} = \frac{1}{4\pi}\iint \boldsymbol{n}(\boldsymbol{r})\cdot[\partial_x\boldsymbol{n}(\boldsymbol{r})\times\partial_y\boldsymbol{n}(\boldsymbol{r})]\,dx\,dy \qquad (1)$$

is directly proportional to the magnitude of the THE [26].

In contrast, the mechanisms responsible for the enhanced anomalous Hall effect (AHE) in topologically trivial spin textures (i.e., without net scalar spin chirality) are not yet well elucidated [27, 28]. Moreover, the AHE in such topologically trivial magnets has generally been assumed to vary monotonically with magnetic field or magnetization. However, recent experiments have revealed that even topologically trivial double-Q ($2Q$) magnetic structures with $N_{\rm sk}=0$ can exhibit a large AHE comparable with that of skyrmion textures, with a nonmonotonic magnetization dependence [29, 30]. These observations challenge the conventional expectation that topologically trivial spin textures (without a net scalar spin chirality) cannot exhibit an AHE larger than that of its ferromagnetic phase within an intrinsic mechanism, indicating the presence of an alternative enhancement mechanism.

These results are also unexpected from a symmetry perspective, since the irreducible representation associated with the magnetic structure of the $2Q$ order in these experiments [29, 30] is distinct from that of a ferromagnetic state. In other words, the $2Q$ magnetic configuration by itself does not belong to an irreducible representation that can induce a finite Berry curvature. It is therefore nontrivial that the AHE in the $2Q$ regime can be strongly enhanced, even exceeding that in the ferromagnetic phase.

In this study, we theoretically propose an alternative mechanism for enhancing the AHE without relying on scalar spin chirality and demonstrate that the in-plane $2Q$ spin structure can significantly enhance the AHE relative to the ferromagnetic phase. We perform theoretical calculations based on the multiorbital Kondo lattice model [31–33], and find that the $2Q$ state develops a large Berry curvature in $\boldsymbol{k}$ space, despite the absence of net scalar spin chirality in real space. We further demonstrate that orbital hybridization caused by the $2Q$ superstructure is the microscopic origin of such enhancement, leading to behavior that is qualitatively distinct from both ferromagnetic and single-Q ($1Q$) states. Furthermore, the AHE in the $2Q$ state exhibits a nonmonotonic dependence on the magnetic field or magnetization, in agreement with the experimental observations in $GdRu_2Si_2$ [29] and $GdRu_2Ge_2$ [30]. Our results thus uncover a fundamental mechanism by which topologically trivial spin textures can host a giant AHE exceeding that of the ferromagnetic phase.

We consider the multiorbital Kondo lattice model [31–33], whose Hamiltonian is given by

$$\mathcal{H} = \sum_{i,i',\ell,\ell',s} t_{ii'}^{\ell\ell'}\, c_{i\ell s}^{\dagger} c_{i'\ell' s} + \lambda\sum_i (l_z\sigma_z)_i + J\sum_i \boldsymbol{\sigma}_i\cdot\boldsymbol{S}_i, \qquad (2)$$

where $c_{i\ell s}^{\dagger}$ ($c_{i\ell s}$) creates (annihilates) an electron at atomic site i, with orbital $\ell\in\{p_x,p_y\}$ and spin $s\in\{\uparrow,\downarrow\}$, on a square lattice. The first term represents the hopping Hamiltonian, where $t_{ii'}^{\ell\ell'}$ denotes the matrix element

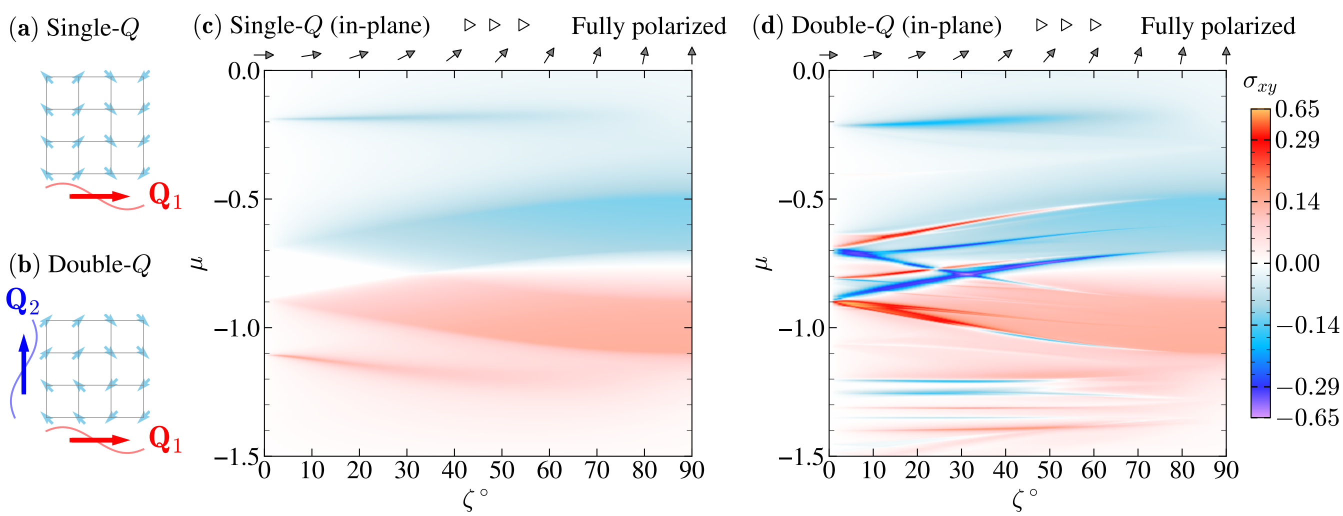

FIG. 1. Panels (a) and (b) illustrate the $1Q$ and $2Q$ spin configurations, respectively. Panels (c) and (d) show the anomalous Hall conductivity σ_{xy} for the $1Q$ and $2Q$ states as functions of the chemical potential μ and the out-of-plane canting angle ζ of the magnetic moments. $\zeta = 0^\circ$ corresponds to coplanar spin configurations, while $\zeta = 90^\circ$ represents a fully polarized configuration. The same color scale is used for panels (c) and (d). For $-1.5 < \mu < 0$, the maximum values of $|\sigma_{xy}|$ are 0.647 for the $2Q$ state and 0.145 for the $1Q$ state. The same figure, plotted over the chemical-potential range $0.5 < \mu < 2.5$, is shown in Fig. 1 of Supplemental Material [34].

from orbital ℓ' at site i' to orbital ℓ at site i. We adopt the Slater-Koster parameters $t_{pp\sigma}$ and $t_{pp\pi}$ for the nearest-neighbor hopping, and $t'_{pp\sigma}$ and $t'_{pp\pi}$ for the next-nearest-neighbor hopping. The second term describes the atomic SOC in the $\{p_x, p_y\}$ subspace, representing the coupling between orbital angular momentum l_z and spin σ_z: $(l_z\sigma_z)_i = \sum_{\ell,\ell',s,s'} \langle \ell|l_z|\ell'\rangle\langle s|\sigma_z|s'\rangle c^\dagger_{i\ell s} c_{i\ell' s'}$; λ is the coupling constant. The third term represents the Kondo coupling with the coupling constant J; $\boldsymbol{S}_i$ denotes the classical localized spin at site i with $|\boldsymbol{S}_i| = 1$. $\boldsymbol{\sigma}_i = \sum_{\ell,s,s'} \langle s|\boldsymbol{\sigma}|s'\rangle\, c^\dagger_{i\ell s} c_{i\ell s'}$ with the vector of Pauli matrices $\boldsymbol{\sigma} = (\sigma^x, \sigma^y, \sigma^z)$ denotes the itinerant electron spin.

For the localized spin configurations $\{\boldsymbol{S}_i\}$, we consider two types of magnetic states. The first is the $1Q$ state with the modulation vector $\boldsymbol{Q}_1 = \pi/2\, \boldsymbol{e}_x$ given by

$$\boldsymbol{S}_i^{1\mathrm{Q}} = (\cos\zeta \sin \mathcal{Q}_{1i},\ \ \cos\zeta\cos\mathcal{Q}_{1i},\ \ \sin\zeta), \tag{3}$$

and the second is the $2Q$ state composed of a sinusoidal superposition of $\boldsymbol{Q}_1$ and $\boldsymbol{Q}_2 = \pi/2\, \boldsymbol{e}_y$, expressed as

$$\boldsymbol{S}_i^{2\mathrm{Q}} = (-\cos\zeta\cos\mathcal{Q}_{2i},\ \ \cos\zeta\cos\mathcal{Q}_{1i},\ \ \sin\zeta), \tag{4}$$

where $\mathcal{Q}_{\nu i} = \boldsymbol{Q}_\nu \cdot (\boldsymbol{r}_i - \boldsymbol{\delta})$ for $\nu = 1, 2$, $\boldsymbol{r}_i$ denotes the position vector, $\boldsymbol{\delta} = (\boldsymbol{e}_x + \boldsymbol{e}_y)/2$ is the phase factor, and $0^\circ \le \zeta \le 90^\circ$ represents the canting angle. At $\zeta = 0^\circ$, $\boldsymbol{S}_i^{1\mathrm{Q}}$ and $\boldsymbol{S}_i^{2\mathrm{Q}}$ correspond to the $1Q$ and $2Q$ spin textures in the xy-plane, as illustrated in Figs. 1(a) and 1(b), respectively. Increasing ζ cants the spins toward the z-direction, leading to noncoplanar spin configurations. Although the scalar spin chirality, $\boldsymbol{S}_i \cdot (\boldsymbol{S}_j \times \boldsymbol{S}_k)$, is locally induced in both states, it vanishes upon spatial averaging, i.e., $N_{\mathrm{sk}} = 0$, indicating that the $1Q$ and $2Q$ states are topologically trivial. At $\zeta = 90^\circ$, both configurations continuously evolve into the fully polarized (FP) ferromagnetic state with $\boldsymbol{S}_i = \boldsymbol{e}_z$. The $1Q$ state is stabilized by the Ruderman-Kittel-Kasuya-Yosida interaction [31, 35–39], while the $2Q$ state is stabilized by additionally taking into account the higher-order multi-spin interactions [40] and magnetic anisotropy [41–43]. Especially, a noncoplanar $2Q$ state with a nonzero ζ has been identified in the skyrmion-hosting materials, such as $GdRu_2Si_2$ [29] and $GdRu_2Ge_2$ [30].

We emphasize that the $1Q$ and $2Q$ magnetic structures defined in Eqs. (3) and (4) transform according to irreducible representations that are distinct from that of the ferromagnetic state, unless the effect of an external magnetic field is explicitly included by setting $\zeta \neq 0$. In the absence of such a field-induced component, these magnetic configurations do not generate Berry curvature on their own. Rather, they act to modulate the magnitude of the AHE that is induced by a finite ferromagnetic moment or by an applied magnetic field. This situation contrasts qualitatively with cases in which antiferromagnetic spin structures transform according to irreducible representations that are symmetry-equivalent to those of a ferromagnetic dipole, as realized in certain noncollinear [44–47] and even collinear magnets [48–51]. In such systems, the magnetic order itself can produce a finite Berry curvature, and hence a spontaneous AHE, even in the absence of net magnetization. In the present work, we instead examine how the $1Q$ and $2Q$ spin textures influence the field-induced AHE. Our analysis reveals a clear distinction between the two: while the $1Q$ state exhibits a conventional, monotonic evolution of the Hall response, the $2Q$ state displays a pronounced enhancement accompanied by a nonmonotonic behavior. We attribute this unconventional response in the $2Q$ phase to multi-Q interference effects inherent to its magnetic structure.

We calculate the anomalous Hall conductivity based on the linear response theory, which is given by

$$\sigma_{xy} = -\frac{e^2}{\hbar}\frac{1}{N}\sum_{n\boldsymbol{k}} f(\mu, E_{n\boldsymbol{k}})\Omega_{xy}^{n\boldsymbol{k}}, \tag{5}$$

where e is the elementary charge, $\hbar$ is the reduced Planck constant, and N denotes the total number of sites. $f(\mu, E_{n\boldsymbol{k}}) = \{1 + \exp[(E_{n\boldsymbol{k}} - \mu)/(k_{\mathrm{B}}T)]\}^{-1}$ denotes the Fermi-Dirac distribution function, where k_{B} is the Boltzmann constant, T is the temperature, and μ is the chemical potential. $\Omega_{xy}^{n\boldsymbol{k}}$ denotes the Berry curvature of the n-th band [52], calculated as

$$\Omega_{xy}^{n\boldsymbol{k}} = -2\hbar^2 \sum_{m\neq n} \frac{\Im[\langle u_{m\boldsymbol{k}}|v_{x,\boldsymbol{k}}|u_{n\boldsymbol{k}}\rangle\langle u_{n\boldsymbol{k}}|v_{y,\boldsymbol{k}}|u_{m\boldsymbol{k}}\rangle]}{(E_{n\boldsymbol{k}} - E_{m\boldsymbol{k}})^2}. \tag{6}$$

Here, $\boldsymbol{v}_{\boldsymbol{k}} \equiv \partial\mathcal{H}_{\boldsymbol{k}}/\partial(\hbar\boldsymbol{k})$ is the velocity operator, and $u_{n\boldsymbol{k}}$ is the periodic part of the Bloch wave function. In the following, the $\boldsymbol{k}$ sum is evaluated on a grid of $\Delta k_x = \Delta k_y = \pi/1024$, the temperature is set to zero, and $\hbar = e = k_{\mathrm{B}} = 1$. Physical units are recovered by multiplying σ_{xy} by $e^2/\hbar$, which corresponds to $243\,\mu$S per 2D layer. Assuming an interlayer spacing on the order of 10 Å, this yields $\sigma_{xy} \sim 2\times 10^3$ S/cm, which is of the typical order of the intrinsic contribution to AHE in ferromagnetic compounds [53].

We evaluate σ_{xy} using the fixed spin configurations in Eqs. (3) and (4), a standard approach to examine its behavior [18, 43]. We set the model parameters as $t_{pp\sigma} = 1$, $t_{pp\pi} = -0.4$, $t'_{pp\sigma} = 0.3$, $t'_{pp\pi} = -0.1$, and $\lambda = 0.05$, and consider the weak-coupling regime by setting $J = 0.2$ unless otherwise noted; the results for other hopping parameters are shown in Supplemental Material [34].

Figures 1(c) and 1(d) show the calculated results of AHE for the $1Q$ and $2Q$ systems, respectively, where the chemical potential is sampled with a uniform spacing of $\Delta\mu = 2\times 10^{-4}$ and the canting angle is sampled with a spacing of $\Delta\zeta = 1^\circ$. For comparison, we use the same color scale in both plots. The maximum values of $|\sigma_{xy}|$ are given by 0.647 for the $2Q$ state and 0.145 for the $1Q$ state. This demonstrates a substantial enhancement of the Hall conductivity in the $2Q$ state compared with the $1Q$ state.

Before discussing the AHE in the $1Q$ and $2Q$ states in detail, we first examine its behavior in the FP state realized at $\zeta = 90^\circ$ in both panels [Fig. 1(c) and (d)]. In this case, σ_{xy} exhibits two broad peaks at $\mu = -1, -0.6$, which correspond to the exchange energy splitting $2J = 0.4$, while their widths are primarily determined by the SOC $2\lambda = 0.1$. This behavior is fully consistent with the conventional mechanism [27, 28], in which the interplay between SOC and ferromagnetic moments generates Berry curvatures of opposite sign for a split Kramers pair [54].

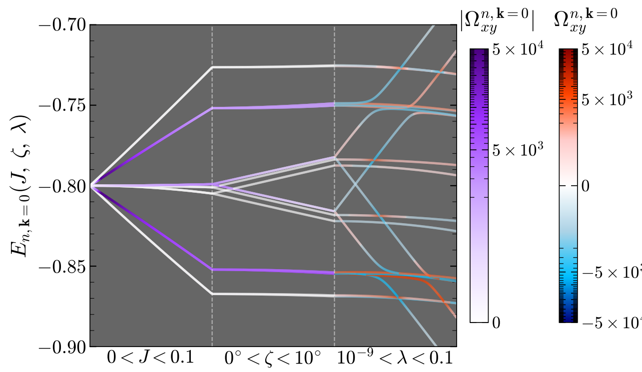

FIG. 2. Berry curvature of the energy eigenstates at the Γ point for the $2Q$ magnetic configuration. The vertical axis denotes the eigenenergy, and the horizontal axis represents the trajectory in the model-parameter space $(J,\ \zeta,\ \lambda)$. Along the parameter path, only one parameter is varied at a time while the others are held fixed: $(J,\ \zeta,\ \lambda) : (0,\ 0^\circ,\ 10^{-9}) \rightarrow (0.1,\ 0^\circ,\ 10^{-9}) \rightarrow (0.1,\ 10^\circ,\ 10^{-9}) \rightarrow (0.1,\ 10^\circ,\ 0.1)$. Violet shading in the region for $0 < J < 0.1$ and $0^\circ < \zeta < 10^\circ$ indicates the absolute value in degenerate regions where contributions cancel, while the blue-to-red colormap is used in the region for $10^{-9} < \lambda < 0.1$ where degeneracy is lifted.

Next, we examine the case of $\zeta < 90^\circ$ in the $1Q$ state. As shown in Fig. 1(c), the behavior of σ_{xy} is not significantly different from that in the ferromagnetic state at $\zeta = 90^\circ$: the two main peaks at $\mu = -1$ and $\mu = -0.6$ move closer together with decreasing ζ, reflecting the reduction of the z-spin component (magnetization). Meanwhile, additional structures appear around $\mu = -1.1$ and $\mu = -0.2$ at small ζ, which originate from the $1Q$ modulations. Their magnitudes are comparable with the ferromagnetic contributions, but they gradually diminish as ζ increases. Thus, the overall behavior remains qualitatively similar to that of the FP state, indicating that it is primarily governed by the interplay between SOC and the net magnetization, although the $1Q$ spiral modulation introduces additional features in σ_{xy} for small ζ.

Compared with the $1Q$ state in Fig. 1(c), the behavior of σ_{xy} changes drastically in the $2Q$ state, as shown in Fig. 1(d). In addition to the features inherited from the $1Q$ state, the $2Q$ state exhibits additional peak structures with pronounced enhancements (up to roughly five times those in the $1Q$ state) and even sign reversals in several regions. In particular, σ_{xy} is strongly enhanced near $\mu = -0.9$ and -0.7, corresponding to the band energies split by the exchange coupling, $E = -0.8 \pm J/2$. Here, the emphasis is not on the magnitude of the σ_{xy} in the $1Q$ state, but rather on the enhancement and unconventional behavior that emerge in the $2Q$ state. As detailed below, this large enhancement originates from gap opening and orbital hybridization induced through electric quadrupolar scattering mechanism under the $2Q$ spin configuration.

To analyze the microscopic origin of the enhanced AHE peak in the $2Q$ state [Fig. 1(d)], we examine the parameter dependence of the $\boldsymbol{k}$-space Berry curvature. In particular, we focus on the Berry curvature at the Γ point near $E = -0.8$, since the $2Q$ contribution in Fig. 1(d) originates from the gaps opened at or near the Γ point (see Fig. 2 of the Supplemental Material [34]). The results are shown in Fig. 2, where we vary three parameters $(J,\ \zeta,\ \lambda)$ in order to discuss the origin of large Berry curvature under the $2Q$ ordering. In the absence of the SOC, the Hall conductivity σ_{xy} vanishes because $2Q$ spin configuration carries no net scalar spin chirality, and each band remains at least doubly degenerate, ensuring that the Berry curvature cancels within each degenerate pair. Remarkably, however, a large Berry curvature of order 10^4 appears as a hidden form in the doubly degenerate bands even for an almost negligible SOC $\lambda = 10^{-9}$, as indicated by the violet region in the range $0 < J < 0.1$, where the $2Q$ spin configuration is characterized by a coplanar arrangement. A similar trend persists for $0^\circ < \zeta < 10^\circ$, where the system hosts a noncoplanar yet topologically trivial spin configuration. This behavior is unique to the $2Q$ state and does not appear in the $1Q$ state, as shown in Supplemental Material [34]. Reflecting this distinction, the application of SOC leads to quantitatively different responses in σ_{xy} for the two states.

The introduction of the SOC in the range for $10^{-9} < \lambda < 0.1$ lifts the band degeneracy and gives rise to pronounced values of the net Berry curvature. The magnitude of the induced Berry curvature is comparable with that found in the degenerate bands, indicating that the giant AHE originates from the large Berry curvature already present within the degenerate manifold. In this sense, the SOC is necessary to render the Berry curvature finite by lifting the band degeneracy; however, it is not crucial for determining its quantitative magnitude. Moreover, the giant Berry curvature embedded within the degenerate bands is a distinctive feature of the $2Q$ state and is absent in the $1Q$ phase. This observation underscores the essential role of multi-Q spin textures in generating such an enhanced Berry curvature response.

A key distinction between the $1Q$ and $2Q$ states lies in the presence or absence of interference between the constituent SDWs. In the $2Q$ state, the spin texture is formed by two modulations with wave vectors $\boldsymbol{Q}_1$ and $\boldsymbol{Q}_2$, whose superposition gives rise to additional spin-scattering channels that strongly affect the conduction electrons. For example, multispin-scattering processes involving both $\boldsymbol{Q}_1$ and $\boldsymbol{Q}_2$ generate quantities at $\boldsymbol{Q}_1 + \boldsymbol{Q}_2$, denoted as $(S^x_{\boldsymbol{Q}_1} S^y_{\boldsymbol{Q}_2})$ ($S^\mu_{\boldsymbol{q}}$ is the Fourier component of the real spin at μ component and wave vector $\boldsymbol{q}$), which correspond—via the exchange interaction J between itinerant electrons and localized spins—to an electric quadrupolar scattering mechanism that hybridizes the p_x and p_y orbitals [55]. Such quadrupolar scattering processes modify the orbital magnetic dipole at $\boldsymbol{Q}_1 + \boldsymbol{Q}_2$, whose matrix elements are the same as the electric quadrupole, thereby inducing substantial modulations of the Berry curvature. Indeed, as shown in the Supplemental Material [34], the behavior of the orbital magnetic dipole at $\boldsymbol{Q}_1 + \boldsymbol{Q}_2$ closely tracks the field and parameter dependence of σ_{xy} in the $2Q$ phase. This correspondence indicates that higher-harmonic orbital hybridization, arising from the interference inherent to the $2Q$ spin texture, is essential for enhancement of the AHE in this phase.

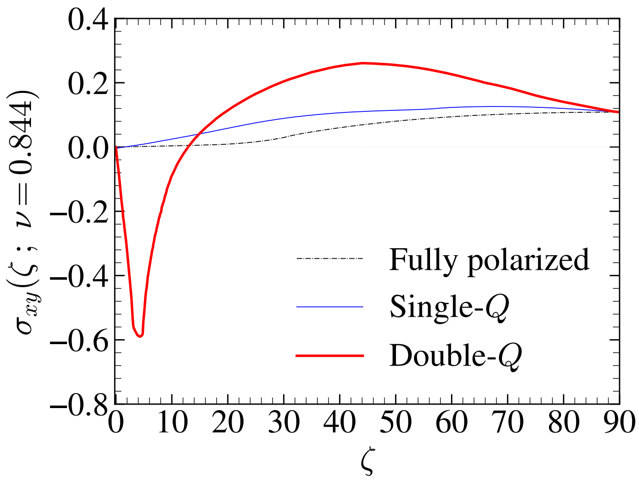

FIG. 3. Anomalous Hall conductivity σ_{xy} as a function of the parameter ζ. The three line plots correspond to the fully polarized (black dash-dotted), $1Q$ (blue solid), and $2Q$ (red bold) magnetic states, respectively. In all cases, the electron filling ratio ν is fixed at 0.84, corresponding to $\mu \simeq 1.77$ for $\zeta = 0^\circ$ (See Fig. 1 of Supplemental Material [34]). The sampling interval for the canting angle ζ is $\Delta\zeta = 1^\circ$ in all cases, except for the $2Q$ configuration in the range $0^\circ < \zeta < 10^\circ$, for which a finer resolution of $\Delta\zeta = 0.1^\circ$ is employed to capture the rapid variation in σ_{xy}.

To further elucidate the unconventional AHE arising from the $2Q$ spin configuration, we examine the dependence of σ_{xy} on the out-of-plane angle ζ (mimicking out-of-plane magnetic field or magnetization) at a fixed electron filling, as shown in Fig. 3. For comparison, we also include the FP configuration $\boldsymbol{S}_{\mathrm{FP}}(x, y) = \sin\zeta\,\boldsymbol{e}_z$. In both the FP state and the $1Q$ state, σ_{xy} increases monotonically with ζ, reflecting the conventional behavior in which the AHE is governed primarily by the net magnetization and its interplay with SOC. The effect in the $1Q$ state is modest, arising only from the gap openings generated by the $1Q$ modulation.

The situation changes qualitatively in the $2Q$ state. Here, σ_{xy} shows a striking nonmonotonic evolution as a function of ζ: it grows rapidly and reaches a maximum near $\zeta \approx 4^\circ$, then oscillates (changing its sign) before converging to the value of the FP state at large ζ. This behavior stands in clear contrast to the trends in the $1Q$ and FP states, reflecting the fact that the $2Q$ spin texture induces a nontrivial reconstruction of the Berry curvature in $\boldsymbol{k}$-space. The origin of the nonmonotonic response can be attributed to the Zeeman-driven shift of Berry curvature hot spots in the electronic structure. As ζ increases, these hot spots move in energy, and the AHE is strongly enhanced when two such hot spots coincide at the Fermi level. Note that in the $1Q$ state, although local gaps are present in the band structure, their energy levels remain largely insensitive to the Zeeman splitting. As a result, the anomalous Hall conductivity evolves monotonically with the canting angle, irrespective of the chemical potential, as demonstrated in Fig. 1(c). Therefore, within our framework, it is unlikely that a $1Q$ modulation alone generates a similar nonmonotonic behavior under an external field.

Such a nonmonotonic dependence of the AHE is consistent with recent experimental observations in skyrmion-hosting materials $GdRu_2Si_2$ and $GdRu_2Ge_2$ [29, 30, 56–62]. In both materials, enhanced AHE has been observed in the high-field region where a $2Q$ spin configuration has been proposed to emerge [30, 56]; ρ_{yx} exhibits a pronounced peak and shows a nonmonotonic dependence on the external magnetic field, which cannot be explained within a conventional AHE mechanism proportional to magnetization. Since experiments have established that the magnetic ordering wave vector remains essentially unchanged under an applied magnetic field, the observed nonmonotonic behavior can be attributed to field-induced spin canting within the magnetic structure. The present results indicate that the $2Q$ state provides a qualitative explanation for the observed nonmonotonic dependence of the AHE on the applied magnetic field, whereas the $1Q$ state fails to capture such behavior. Although the minimal model considered here differs from the complex electronic structures of $GdRu_2Si_2$ and $GdRu_2Ge_2$, which involve both d- and f-electron degrees of freedom, our results demonstrate that the essential nonmonotonic behavior can already emerge from a $2Q$ magnetic structure itself, without invoking detailed or material-specific band-structure effects.

To summarize, we show that a large intrinsic AHE can arise even in a topologically trivial spin texture with $2Q$ spin modulations. Employing the multiorbital Kondo lattice model, we demonstrate that the enhanced AHE appears only in the $2Q$ state, in clear contrast to the FP and $1Q$ spiral states. We further show that higher-order spin-scattering processes inherent to the $2Q$ spin texture induce effective orbital hybridization—as evidenced by the orbital angular momentum at $\boldsymbol{Q}_1 + \boldsymbol{Q}_2$—which in turn produces the Berry curvature hot spots responsible for the enhanced AHE.

We also find that the AHE induced by the $2Q$ spin texture exhibits a nonmonotonic dependence on magnetization. This behavior distinguishes it from the behavior of the $1Q$ spin texture and FP state and is consistent with experimental observations in $GdRu_2Si_2$ and $GdRu_2Ge_2$. These results highlight multi-Q interference as an effective mechanism for realizing large AHEs beyond conventional topological or ferromagnetic origins.

This research was supported by JSPS KAKENHI Grants Numbers JP22H00101, JP22H01183, JP23H04869, JP23K03288, JP23K20827, and by JST CREST (JPMJCR23O4) and JST FOREST (JPMJFR2366).

Data availability. The data that support the findings of this article are openly available in Zenodo at https://zenodo.org/records/19717698.

[1] P. Bak and B. Lebech, Phys. Rev. Lett. **40**, 800 (1978).
[2] Y. A. Izyumov, Soviet Physics Uspekhi **27**, 845 (1984).
[3] K. A. McEwen and M. B. Walker, Phys. Rev. B **34**, 1781 (1986).
[4] B. Binz, A. Vishwanath, and V. Aji, Phys. Rev. Lett. **96**, 207202 (2006).
[5] B. Binz and A. Vishwanath, Phys. Rev. B **74**, 214408 (2006).
[6] N. Nagaosa and Y. Tokura, Nat. Nanotechnol. **8**, 899 (2013).
[7] B. Göbel, I. Mertig, and O. A. Tretiakov, Physics Reports **895**, 1 (2021), beyond skyrmions: Review and perspectives of alternative magnetic quasiparticles.
[8] S. Hayami and R. Yambe, Mater. Today Quantum **3**, 100010 (2024).
[9] T. Holstein and L. Friedman, Phys. Rev. **165**, 1019 (1968).
[10] P. Bruno, V. K. Dugaev, and M. Taillefumier, Phys. Rev. Lett. **93**, 096806 (2004).
[11] D. Loss and P. M. Goldbart, Phys. Rev. B **45**, 13544 (1992).
[12] J. Ye, Y. B. Kim, A. J. Millis, B. I. Shraiman, P. Majumdar, and Z. Tešanović, Phys. Rev. Lett. **83**, 3737 (1999).
[13] K. Ohgushi, S. Murakami, and N. Nagaosa, Phys. Rev. B **62**, R6065 (2000).
[14] R. Shindou and N. Nagaosa, Phys. Rev. Lett. **87**, 116801 (2001).
[15] G. Tatara and H. Kawamura, Journal of the Physical Society of Japan **71**, 2613 (2002).
[16] A. Neubauer, C. Pfleiderer, B. Binz, A. Rosch, R. Ritz, P. G. Niklowitz, and P. Böni, Phys. Rev. Lett. **102**, 186602 (2009).
[17] N. Kanazawa, Y. Onose, T. Arima, D. Okuyama, K. Ohoyama, S. Wakimoto, K. Kakurai, S. Ishiwata, and Y. Tokura, Phys. Rev. Lett. **106**, 156603 (2011).
[18] K. Hamamoto, M. Ezawa, and N. Nagaosa, Phys. Rev. B **92**, 115417 (2015).
[19] B. Göbel, A. Mook, J. Henk, and I. Mertig, Phys. Rev. B **95**, 094413 (2017).
[20] T. Kurumaji, T. Nakajima, M. Hirschberger, A. Kikkawa, Y. Yamasaki, H. Sagayama, H. Nakao, Y. Taguchi, T. hisa Arima, and Y. Tokura, Science **365**, 914 (2019).
[21] S. Mühlbauer, B. Binz, F. Jonietz, C. Pfleiderer, A. Rosch, A. Neubauer, R. Georgii, and P. Böni, Science **323**, 915 (2009).
[22] X. Z. Yu, Y. Onose, N. Kanazawa, J. H. Park, J. H. Han, Y. Matsui, N. Nagaosa, and Y. Tokura, Nature **465**, 901 (2010).
[23] N. Romming, C. Hanneken, M. Menzel, J. E. Bickel, B. Wolter, K. von Bergmann, A. Kubetzka, and R. Wiesendanger, Science **341**, 636 (2013).

[24] A. Fert, V. Cros, and J. ao Sampaio, Nature Nanotechnology **8**, 152 (2013).
[25] A. Fert, N. Reyren, and V. Cros, Nature Reviews Materials **2**, 17031 (2017).
[26] N. Verma, Z. Addison, and M. Randeria, Science Advances **8**, eabq2765 (2022).
[27] N. Nagaosa, J. Sinova, S. Onoda, A. H. MacDonald, and N. P. Ong, Rev. Mod. Phys. **82**, 1539 (2010).
[28] D. Xiao, M.-C. Chang, and Q. Niu, Rev. Mod. Phys. **82**, 1959 (2010).
[29] N. D. Khanh, T. Nakajima, X. Yu, S. Gao, K. Shibata, M. Hirschberger, Y. Yamasaki, H. Sagayama, H. Nakao, L. Peng, K. Nakajima, R. Takagi, T. hisa Arima, Y. Tokura, and S. Seki, Nature Nanotechnology **15**, 444 (2020).
[30] H. Yoshimochi, R. Takagi, J. Ju, N. D. Khanh, H. Saito, H. Sagayama, H. Nakao, S. Itoh, Y. Tokura, T. Arima, S. Hayami, T. Nakajima, and S. Seki, Nature Physics **20**, 1001 (2024).
[31] T. Kasuya, Progress of Theoretical Physics **16**, 45 (1956).
[32] J. Kondo, Progress of Theoretical Physics **32**, 37 (1964).
[33] H. Tsunetsugu, M. Sigrist, and K. Ueda, Rev. Mod. Phys. **69**, 809 (1997).
[34] See Supplemental Material for details on the momentum-space distribution of Berry curvature in the electronic band structure, the dependence of the results on hopping parameters and magnetic modulation vectors, and the enhancement of Berry curvature by the orbital density wave.
[35] M. A. Ruderman and C. Kittel, Phys. Rev. **96**, 99 (1954).
[36] K. Yosida, Phys. Rev. **106**, 893 (1957).
[37] A. Yoshimori, J. Phys. Soc. Jpn. **14**, 807 (1959).
[38] T. A. Kaplan, Phys. Rev. **124**, 329 (1961).
[39] R. J. Elliott, Phys. Rev. **124**, 346 (1961).
[40] S. Hayami, R. Ozawa, and Y. Motome, Phys. Rev. B **95**, 224424 (2017).
[41] S. Hayami and R. Yambe, J. Phys. Soc. Jpn. **89**, 103702 (2020).
[42] O. I. Utesov, Phys. Rev. B **103**, 064414 (2021).
[43] Z. Wang, Y. Su, S.-Z. Lin, and C. D. Batista, Phys. Rev. B **103**, 104408 (2021).
[44] H. Chen, Q. Niu, and A. H. MacDonald, Phys. Rev. Lett. **112**, 017205 (2014).
[45] S. Nakatsuji, N. Kiyohara, and T. Higo, Nature **527**, 212 (2015).
[46] M.-T. Suzuki, T. Koretsune, M. Ochi, and R. Arita, Phys. Rev. B **95**, 094406 (2017).
[47] J.-R. Soh, F. de Juan, N. Qureshi, H. Jacobsen, H.-Y. Wang, Y.-F. Guo, and A. T. Boothroyd, Phys. Rev. B **101**, 140411 (2020).
[48] I. V. Solovyev, Phys. Rev. B **55**, 8060 (1997).
[49] L. Šmejkal, R. González-Hernández, T. Jungwirth, and J. Sinova, Sci. Adv. **6**, eaaz8809 (2020).
[50] M. Naka, S. Hayami, H. Kusunose, Y. Yanagi, Y. Motome, and H. Seo, Phys. Rev. B **102**, 075112 (2020).
[51] S. Hayami and H. Kusunose, Phys. Rev. B **103**, L180407 (2021).
[52] Y. Yao, L. Kleinman, A. H. MacDonald, J. Sinova, T. Jungwirth, D.-s. Wang, E. Wang, and Q. Niu, Phys. Rev. Lett. **92**, 037204 (2004).
[53] S. Onoda, N. Sugimoto, and N. Nagaosa, Phys. Rev. B **77**, 165103 (2008).
[54] S. Ohgata and S. Hayami, Phys. Rev. B **112**, 014421 (2025).
[55] S. Hayami and Y. Motome, Phys. Rev. B **104**, 144404 (2021).
[56] N. D. Khanh, T. Nakajima, S. Hayami, S. Gao, Y. Yamasaki, H. Sagayama, H. Nakao, R. Takagi, Y. Motome, Y. Tokura, T.-h. Arima, and S. Seki, Advanced Science **9**, 2105452 (2022).
[57] Y. Yasui, C. J. Butler, N. D. Khanh, S. Hayami, T. Nomoto, T. Hanaguri, Y. Motome, R. Arita, T. hisa Arima, Y. Tokura, and S. Seki, Nature Communications **11**, 5925 (2020).
[58] N. Matsuyama, T. Nomura, S. Imajo, T. Nomoto, R. Arita, K. Sudo, M. Kimata, N. D. Khanh, R. Takagi, Y. Tokura, S. Seki, K. Kindo, and Y. Kohama, Phys. Rev. B **107**, 104421 (2023).
[59] G. D. A. Wood, D. D. Khalyavin, D. A. Mayoh, J. Bouaziz, A. E. Hall, S. J. R. Holt, F. Orlandi, P. Manuel, S. Blügel, J. B. Staunton, O. A. Petrenko, M. R. Lees, and G. Balakrishnan, Phys. Rev. B **107**, L180402 (2023).
[60] S. Eremeev, D. Glazkova, G. Poelchen, A. Kraiker, K. Ali, A. V. Tarasov, S. Schulz, K. Kliemt, E. V. Chulkov, V. Stolyarov, *et al.*, Nanoscale Adv. **5**, 6678 (2023).
[61] Y. Dong, Y. Kinoshita, M. Ochi, R. Nakachi, R. Higashinaka, S. Hayami, Y. Wan, Y. Arai, S. Huh, M. Hashimoto, D. Lu, M. Tokunaga, Y. Aoki, T. D. Matsuda, and T. Kondo, Science **388**, 624 (2025).
[62] B. M. Huddart, A. Hernández-Melián, G. D. A. Wood, D. A. Mayoh, M. Gomilšek, Z. Guguchia, C. Wang, T. J. Hicken, S. J. Blundell, G. Balakrishnan, and T. Lancaster, Phys. Rev. B **111**, 054440 (2025).